J Nanopart Res (2019) 21: 221
https://doi.org/10.1007/s11051-019-4670-7

RESEARCH PAPER

Fabrication of p-NiO nanoparticles/n-TiO_2 nanospheres photocatalysts and their photocatalytic performance for degradation of Rh B

Zheng Liang · Junqi Li · Xuanmeng He · Lijun Niu · Xiaotao Xu

Received: 13 April 2019 / Accepted: 25 September 2019 / Published online: 28 October 2019

Abstract The p-n junction structure has been regarded as an effective strategy to improve the photocatalytic activity due to their effectively separation of photoelectron-holes. In the paper, the p-NiO nanoparticles/n-TiO_2 nanosphere photocatalysts were successfully fabricated by the hydrothermal method. The structure and morphology of the photocatalysts with p-n junction were systematically characterized by XRD, XPS, SEM, TEM, and UV-vis. And the photocatalytic performance of the photocatalysts was evaluated by the photocatalytic decomposition of Rh B under ultraviolet light irradiation. The results showed that the loading content of NiO nanoparticles in p-n junction had influence on their photocatalytic activity. And the optimal NiO loading content for p-n junction photocatalysts was determined. After the photodegradation of Rh B under UV irradiation for 70 min, the degradation rates of the TiO_2@NiO-8 samples were reached to about 97.9%. The enhanced photocatalytic performance of the TiO_2@NiO composites was attributed to the formation of p-n junction at interfacial interaction between NiO nanoparticles and TiO_2 nanospheres, which promoted the effectively separation of photo electron-holes. Moreover, the photocatalytic mechanisms of the p-NiO nanoparticles/n-TiO_2 nanospheres photocatalysts in the degradation processes were elucidated.

Keywords p-n junction structure · p-NiO nanoparticles/n-TiO_2 nanospheres · Photocatalyst

Electronic supplementary material The online version of this article (https://doi.org/10.1007/s11051-019-4670-7) contains supplementary material, which is available to authorized users.

Z. Liang · J. Li · X. He · L. Niu · X. Xu
School of Materials Science and Engineering, Shaanxi University of Science & Technology, Xi'an 710021, China

Z. Liang · J. Li · X. He (✉) · L. Niu · X. Xu
School of Material Science and Engineering, Shaanxi Key Laboratory of Green Preparation and Functionalization for Inorganic Materials, Shaanxi University of Science and Technology, Xi'an 710021, China
e-mail: hexuanmeng@sust.edu.cn

Introduction

Semiconductor-based photocatalytic oxidation is considered to an effective way for the environment remediation (Vimonses et al. 2010; Yap and Lim 2011; Chen et al. 2009). TiO_2 is a promising semiconductor material, which can be applied in photoelectrodes (Yu et al. 2014a, b), environmental purification (Xian et al. 2014), and solar cells (Yu et al. 2014a, b) due to its high stability, non-toxic, and safety toward humans (Gupta et al. 2011). Therefore, TiO_2-based materials have attracted considerable attentions in the field of semiconductor photocatalysis. However, the narrow light response range and high recombination rate of photoelectron-holes of the TiO_2 based photocatalyst limited their application in some extent (Jiang et al. 2011). Therefore, many methods have been explored to improve the photoelectron-hole separation efficiency and widen the light response range, such as ion doping (Oropeza and Egdell 2011; Wang et al. 2019), coupled semiconductor (Wang et al. 2009; Bastian et al. 2018),

and deposition of noble metal (Rupa et al. 2009; Laguna et al. 2019). Coupled semiconductor photocatalyst has recently received more attentions due to its high photoelectron-hole separation efficiency and wide spectral response (Huang et al. 2019; Sun et al. 2015a, b; Sun et al. 2017). Especially, the coupled semiconductor combined with nanoparticles materials possessing a larger specific surface area can lead to a stronger adsorption capacity as well as a better photocatalytic performance.

It has been found that (ZnO, SnO_2, NiO)/TiO_2 hybrid semiconductor could obviously suppress the recombination of photogenerated electron-hole, prolong their lifetime, and significantly enhance the photocatalytic activity (Wang et al. 2017; Fang et al. 2017). Among various transition metal oxides, NiO has been extensively investigated due to its interesting 3D electronic structure, which are localized in space but spread out over a wide energy range because of strong coulomb repulsion between them (Wang et al. 2017). This unique electronic distribution leads to high mobility of charge carriers in NiO, making it as a cocatalyst in the photocatalytic water splitting, dye-sensitized solar cells (Wang et al. 2016). Moreover, NiO is an ideal p-type semiconductor material, which has superior performance and low cost. It is an ideal candidate to form a p-n junction with TiO_2 (Wang et al. 2017; Fang et al. 2017). The p-n junction could be formed by the recombination of a p-type semiconductor and an n-type semiconductor, which can improve the separation of photogenerated carriers (Khun et al. 2013). Nevertheless, NiO is generally reported as a wide band gap semiconductor with Eg = ~ 3.5 eV, precluding it from absorbing visible light, which can be used as a suitable candidate for surface modification materials of TiO_2 (Gonçalves et al. 2017; Hou et al. 2016). On the other hand, assembling p-type semiconductor NiO nanoparticles on the surface of n-type TiO_2 nanobelts has been recently reported, displaying an excellent visible light response (Lin et al. 2011; Vinoth et al. 2016). Therefore, it is possible to optimize the optical property of assembling NiO nanoparticles. Therefore, developing a new category of p-n junction photocatalyst for NiO/TiO_2 is highly desirable for their enhanced photocatalytic performance.

In this work, we synthesized TiO_2 microspheres by controlling hydrolysis of TBOT in ethanol solution. And then, TiO_2@$Ni(HCO_3)_2$ was obtained through coating $Ni(HCO_3)_2$ on the surface of the TiO_2 microspheres by a hydrothermal method. Finally, the TiO_2@NiO p-n junction photocatalysts were prepared by calcination of the prepared TiO_2@$Ni(HCO_3)_2$ at different temperatures. And the optimal NiO loading content for p-n junction photocatalysts was determined. Under UV irradiation to photodegradation Rh B for 70 min, the degradation rates of the TiO_2@NiO-8 samples were reached to about 97.9%. The enhanced photocatalytic performance of the TiO_2@NiO composites was attributed to the formation of p-n junction at interfacial interaction between NiO nanoparticles and TiO_2 nanospheres, which promoted the effectively separation of photo electron-holes.

Experimental

Materials

Tetrabutyltitanate (TBOT, A.R.) was purchased from Beijing Chemical Reagent Co. Led., China; nickel nitrate heahydrate ($Ni(NO_3)_2 \cdot 6H_2O$, A.R.) and potassium chloride (KCl, A.R.) were obtained from Sinopharm Chemical Reagent Co. Led. Urea (H_2NCONH_2) and ethanol were purchased from Tianjin Eu Chen Chemical Reagent Co. Led., China. Deionized water was used throughout our experiments.

Preparation of TiO_2 microspheres

The TiO_2 microspheres were synthesized by controlling hydrolysis of TBOT in ethanol. In a typical synthesis, 1.2 mL of KCl aqueous solution (0.4 mM) was mixed with 300 mL of ethanol under vigorously stirring. After stirring for 20 min, 5 mL of TBOT was added drop by drop into the mixture under continuously stirring. The stirring was ceased until the mixture became the white suspension and then aged at a dry atmosphere. After aging for 4 h, the reactions were finished and the white precipitates were collected by centrifugation and washed with ethanol and deionized water for several times. Finally, the as-prepared white powders were dried at 70 °C for 12 h and the TiO_2 microspheres were obtained.

Preparation of TiO_2@NiO composite photocatalyst

TiO_2@NiO composite photocatalyst was synthesized by hydrothermal combining with calcination process. 0.2 g TiO_2 as-prepared microspheres was ultrasonically

dispersed into 120 mL deionized water. Then, different amount of $Ni(NO_3)_2 \cdot 6H_2O$ and urea were added into the above suspension, stirring for 30 min at room temperature. Subsequently, the 70 mL of suspensions was transferred into 100-mL Teflon autoclave and kept at 120 °C for 12 h. After cooling down to room temperature, the precipitation was collected by centrifugation and washed with absolute ethanol and deionized water for three times. Then, the precipitation was dried at 60 °C overnight. Finally, the dried powders were calcined at various temperatures (400 °C, 500 °C, and 600 °C) for 3 h in air. The samples were recorded as TiO_2@NiO-x, and the x was referred to the adding amount of $Ni(NO_3)_2 \cdot 6H_2O$. The sample TiO_2@NiO-8 which was calcined at 400 °C, 500 °C, and 600 °C for 3 h were labeled to TiO_2@NiO-400, TiO_2@NiO-500, and TiO_2@NiO-600 (TiO_2@NiO-8 the same as TiO_2@NiO-500).

Preparation of NiO samples

0.008 g $Ni(NO_3)_2 \cdot 6H_2O$ and 2 g urea were added into 120 mL deionized water, stirring for 30 min at room temperature. Subsequently, the 70 mL of suspensions was transferred into 100-mL Teflon autoclave and kept at 120 °C for 12 h. Then, the precipitation was dried at 60 °C overnight. Finally, the dried powders were calcined at 500 °C for 3 h in air. The samples were recorded as NiO.

Characterization

The phase composition and degree of crystallization of the sample were analyzed by Rigaku X-ray diffractometer (D/Max-2200PC). The crystal morphologies of the samples were examined with field-emission scanning electron microscopy (SEM) using a Hitachi S4800 microscope and equipped with an energy dispersive X-ray spectrometer (EDS). The morphology of the products was also characterized by a transmission electron microscope (JEM 2010 from JEOL, Japan) operated at 200 kV. The surface electronic state was analyzed by X-ray photoelectron spectroscopy (XPS, ESCALAB 250Xi). The UV-vis absorbance spectra were recorded on a spectrophotometer (Lambda-950, PerkinElmer), and $BaSO_4$ was used as a reflectance sample.

Measurements of electrochemical performance

The transient photocurrent responses and EIS measurements were conducted on an electrochemical system (CHI-760e, Shanghai Chenhua) by using a three-electrode electrochemical system including Pt wire and Ag/AgCl electrode as the counter electrode and the reference electrode, respectively.

Measurements of photocatalytic activities

The degradation of Rh B was performed to evaluate the photocatalytic performance of TiO_2@NiO. Firstly, the 0.01 g TiO_2@NiO photocatalyst was added into 10 mL Rh B (10 mg/L) solution. Then, the mixture was transferred to the quartz photoreactors and ultrasonic for 30 min in the dark condition to achieve adsorption-desorption equilibrium. The mercury lamp of 500 W was used as the ultraviolet light source and the circulating cooling water device was used to ensure that the test process was performed at a constant temperature. A part of suspension was removed at the same time interval and the supernatant was collected by centrifugation with the speed of 3500 r/min. Then, the UV-vis spectrophotometer (Lambda-950, PerkinElmer, USA) was used to record the changes in the absorbance at 553 nm.

Results and discussion

The XRD patterns were performed to analyze the crystal structure and phase composition of the materials. Figure 1 showed the XRD patterns of TiO_2@NiO-8 calcined at different temperature in air atmosphere. The diffraction peaks of the anatase TiO_2 (JCPDS card no. 21-1272) and bunsenite NiO (JCPDS card no. 47-1049) were detected in all samples. Compared with the TiO_2@NiO-400, the TiO_2@NiO-500 presented more sharp diffraction peaks, which indicated that TiO_2@NiO-500 sample had higher crystallinity. In addition, two peaks at 33.1° and 35.6° were exhibited in the TiO_2@NiO-600, which correspond to the (104) and (110) planes of $NiTiO_3$ (JCPDS card no. 33-0960) (He et al. 2018). The fact indicated that the impurity phase of $NiTiO_3$ existed in the TiO_2@NiO-600. Therefore, the calcination temperature of TiO_2@NiO photocatalyst was selected at 500 °C.

Figure 2 showed the XRD patterns of TiO_2@NiO-8 before calcination, and the patterns of pure NiO and

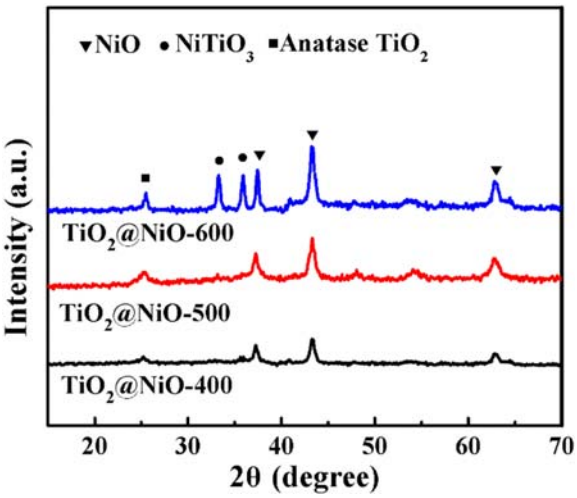

Fig. 1 XRD patterns of TiO_2@NiO-400, TiO_2@NiO-500, and TiO_2@NiO-600

anatase TiO_2 were used as comparison. It can be seen that the patterns of $Ni(HCO_3)_2$ indexed to JCPDS card no. 15-0782 were detected in TiO_2@NiO-8 before calcination. In the synthesis process, the Ni^{2+} was deposited on the surface of titanium oxide in the form of $Ni(HCO_3)_2$, which were different with our previous report (He X et al. 2018), and the core of TiO_2 was still amorphous. After calcination at 500 °C, the core of TiO_2 was transformed to anatase (as shown in Fig. 1b), which was consistent with the patterns of the pure TiO_2 contrast sample. Meanwhile, the $Ni(HCO_3)_2$ were decomposed into NiO, CO_2, and H_2O, which were evaporated and only the NiO were deposited on the surface of anatase TiO_2. The results indicated that the NiO were successfully synthesized on the surface of TiO_2 microsphere.

The SEM images of pure TiO_2, NiO, and TiO_2@NiO-8 were shown in Fig. 3. As shown in Fig. 3a, the diameter of the TiO_2 microsphere was about 600 nm and with a rough surface. This rough surface was beneficial to the loading of NiO particles. Figure 3b showed the SEM images of pure NiO without TiO_2. It can be seen that the NiO nanoparticles aggregated together, whose dispersity was inferior to that of TiO_2@NiO-8. In Fig. 3c, there are many small particles loaded on the surface of TiO_2@NiO-8 photocatalyst. In order to confirm the formation of Ni species on the TiO_2 surface, the SEM-EDS elemental maps of the TiO_2@NiO-8 were further used to identify the element distribution. As shown in Fig. 3d, the EDS showed that three elements (Ti (green), Ni (blue), and O (red)) were homogeneously distributed in the TiO_2@NiO-8, which confirmed the formation of Ni compound. The above results indicated that the NiO particles were uniformly adhered to the surface of the TiO_2 microspheres.

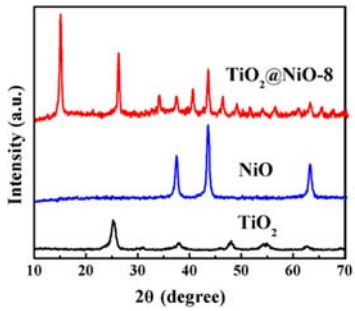

Fig. 2 XRD patterns of TiO_2@NiO-8 before calcination, pure NiO, and TiO_2

The adding amounts of $Ni(NO_3)_2{\cdot}6H_2O$ affected the morphology of TiO_2@NiO photocatalyst. The SEM images of TiO_2@NiO-x (2, 4, 6, 8, 10, and 15) were shown in Fig. 4. As shown in Fig. 4, the average diameter of the TiO_2@NiO was approximately 800 nm. For the samples of TiO_2@NiO-2, TiO_2@NiO-4, and TiO_2@NiO-6, some TiO_2 microspheres were incompletely encapsulated and the size of the nanoparticles of NiO was unevenly distributed (as shown in Fig. 4a, b, c), and some microspheres were aggregated together. However, the microspheres of TiO_2@NiO-8 were well dispersed (as shown in Fig. 4d). The morphology of monomer microspheres was perfectly regular, which could increase the contact area and absorption between the sample and the Rh B. As shown in Fig. 4e and f, the TiO_2@NiO-10 and TiO_2@NiO-15 presented the extremely irregular morphologies. The sizes of the microspheres were unevenly distributed and some nanoparticles were loosely packed on the surface. These imaging data suggest that the NiO were well combined with TiO_2 in TiO_2@NiO-8 photocatalyst.

In order to further confirm the formation of NiO on the TiO_2 surface, the TEM analysis had been used to investigate the crystal structure of TiO_2@NiO-8. The micromorphology was shown in Fig. 5a and b. It can be seen that the morphology of TiO_2@NiO-8 was a homogeneous spheroid structure with the diameter of about 800 nm and the rough particles in the outer layer were clearly visible. Figure 5c showed the HRTEM of TiO_2@NiO-8 photocatalyst and the lattice fringes of NiO and TiO_2 in the photocatalyst, which can be clearly seen. Both the lattice fringes of 0.208 nm and 0.237 nm corresponded well to (004) planes of NiO (JCPDS card no. 47-1049) and (004) plane of anatasephase of TiO_2

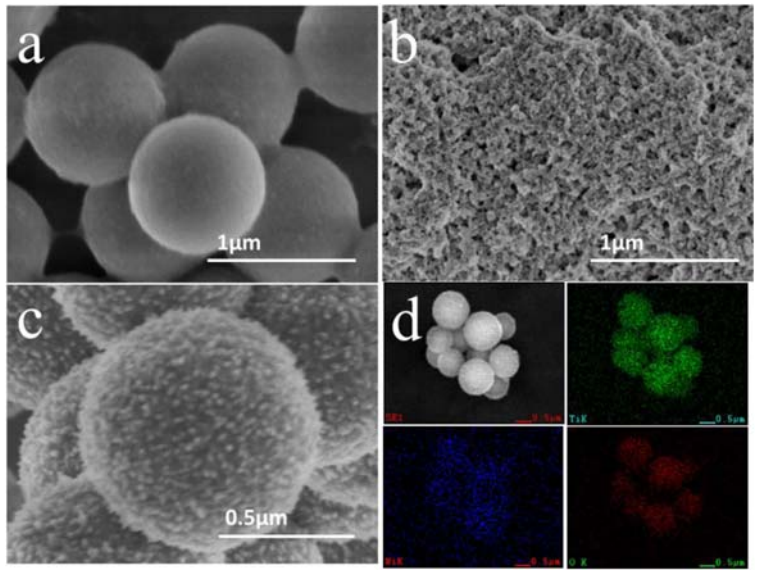

Fig. 3 SEM images of TiO_2 (**a**), NiO (**b**), and TiO_2@NiO-8 (**c**) and the EDX spectrum and elemental mapping of TiO_2@NiO-8 (**d**). Green, blue, and red represent Ti, Ni, and O elements, respectively

(JCPDS card no. 21-1272), respectively. Furthermore, there were some crossing lattice fringes in Fig. 5c (area of red rectangle), from which we could see that NiO nanoparticles were well combined with TiO_2 microsphere. Figure 5d showed the selected area electron diffraction (SAED) pattern of TiO_2@NiO-8 corresponding to the marked region in Fig. 5c. The results confirmed the existence of NiO on the surface of TiO_2 microsphere, and the TiO_2@NiO photocatalyst had been successfully synthesized.

In order to further detect the chemical composition of the sample and the valence state of each element, the XPS analysis of TiO_2, TiO_2@NiO-8, and NiO was performed. The Ti 2p spectra of TiO_2 and TiO_2@NiO-8 photocatalyst were shown in Fig. 6. The binding energy peaks at 458.6 eV and 464.3 eV were assigned to Ti $2p_{3/2}$ and Ti $2p_{1/2}$, corresponding to Ti^{4+} in TiO_2 and the Ti–O bond, respectively (Liu et al. 2014a, b). In contrast to the TiO_2, the TiO_2@NiO-8 displayed a binding energy shift toward high energy for Ti, which should be caused by the incorporation of NiO in the TiO_2@NiO-8 system through the formation of p-n heterojunctions between the NiO and TiO_2 (Wang et al. 2015). Figure 6b showed the high-resolution

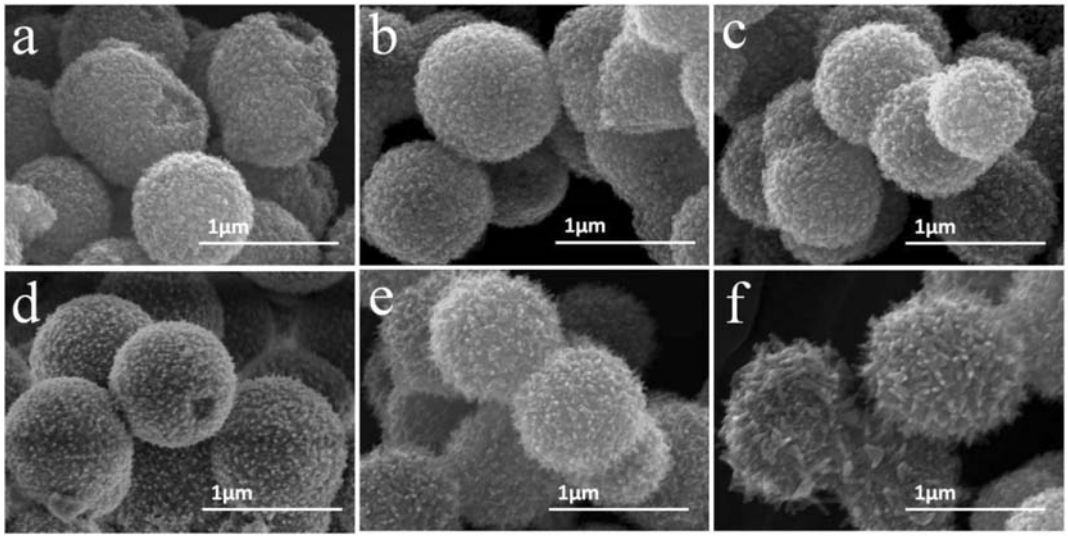

Fig. 4 SEM images of TiO_2@NiO-2 (**a**), TiO_2@NiO-4 (**b**), TiO_2@NiO-6 (**c**), TiO_2@NiO-8 (**d**), TiO_2@NiO-10 (**e**), and TiO_2@NiO-15 (**f**)

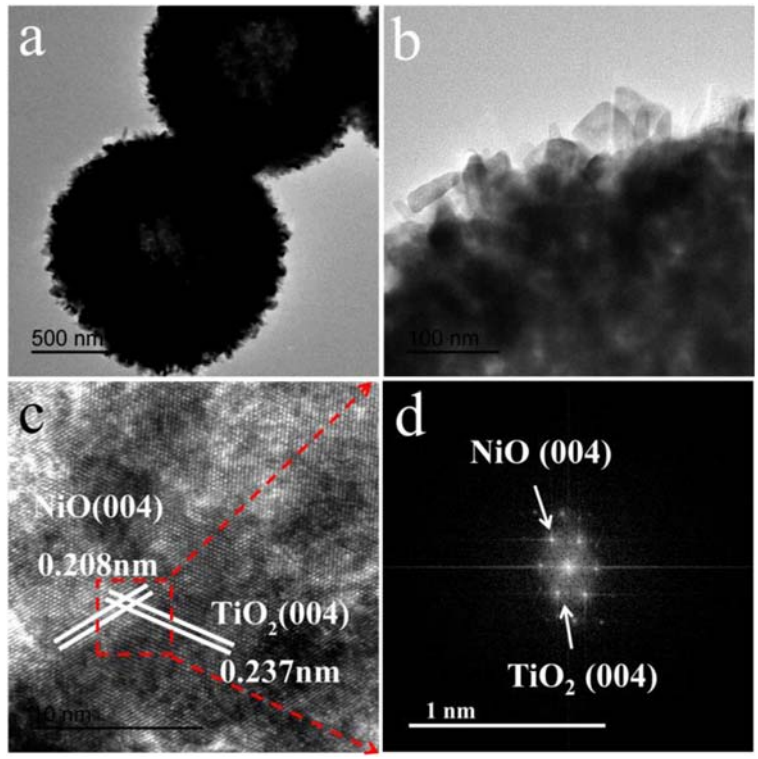

Fig. 5 TEM images and SAED image of the TiO_2@NiO-8 calcination at 500 °C

spectra of the Ni 2p electrons of TiO_2@NiO-8 and NiO. The two characteristic peaks at binding energy of 853.7 eV and 871.7 eV correspond to Ni $2p_{3/2}$ and Ni $2p_{1/2}$, respectively, which coincide with the characteristic peak of Ni^{2+} (Mcintyre and Cook 1975). In addition, it is observed that there is a lower satellite peak at the right of each characteristic peak of Ni, which occurs when Ni^{2+} is in a high spin state (Fominykh et al. 2017), which indicated that NiO samples were successfully loaded in the surface of TiO_2. The O 1s spectra of TiO_2, TiO_2@NiO-8, and NiO can be fitted into a main peak at about 529.7 eV, which is assigned to oxygen atoms bound to metals and a higher binding energy of about 531.6 eV attributed to the surface ·OH species, which is caused by the intrinsic oxygen vacancies of the surface (Fig. 6c) (Zhang et al. 2013). Hence, these results indicated that the p-NiO nanoparticles/n-TiO_2 microspheres samples were successfully prepared (Wang et al. 2015, Cao et al. 2011, Chen et al. 2008).

UV-vis absorption was an important affecting factor for the photocatalytic performance. The typical UV-vis absorption spectra of TiO_2@NiO-400, TiO_2@NiO-500, and TiO_2@NiO-600 were shown in Fig. 7a. All samples had extremely high intensity of light response in the ultraviolet region due to the characteristics of TiO_2. The spectral responded strength of the TiO_2@NiO-500 in the ultraviolet region was much higher than that of TiO_2@NiO-400 and TiO_2@NiO-600. The absorption edge "red shift" of the TiO_2@NiO-500 was also larger than other samples, which indicate that TiO_2@NiO-500 had the more wide light response range. Figure 7b showed the band gap of sample calcined at 400 °C, 500 °C, and 600 °C, which were calculated from formula 3-1.

$$\left(\frac{\alpha h\upsilon}{K}\right)^2 = h\upsilon - E_g \qquad (3-1)$$

By comparison, the band gap of samples calcined at 500 °C was narrowest. Therefore, the TiO_2@NiO-500 has the higher light absorption and narrower band gap, which promoted the enhancement of photocatalytic properties.

The UV-vis diffuse reflectance spectrum of the samples of NiO and TiO_2@NiO-x(x = 0, 2, 4, 6, 10) calcined at 500 °C was displayed in Fig. 8. In the spectral curve of the pure-TiO_2, a strong absorption band was

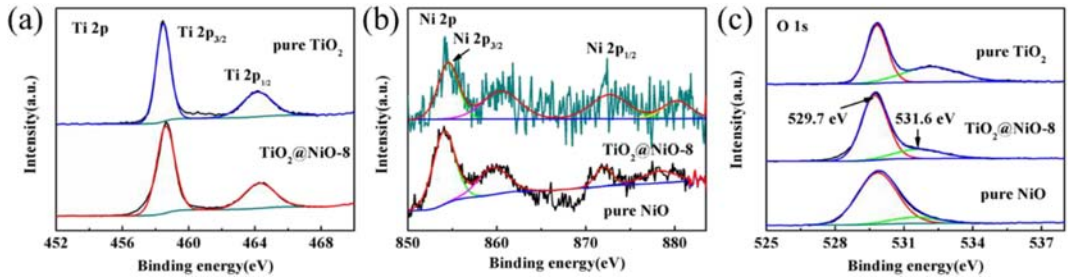

Fig. 6 The XPS spectra of Ti 2p (**a**), Ni 2p (**b**), and O 1s (**c**) for TiO_2, TiO_2@NiO-8, and NiO

observed in the low wavelength region of 200–380 nm, which was owing to the electrons of the valence band O 2p excited to the energy level of the conduction band Ti 3d. The TiO_2 existed in the form of the tetrahedral Ti^{4+} structure and the band gap width was about 3.3 eV (Pham and Lee 2014; Pan et al. 2013). However, the stronger light absorption performances of all TiO_2@NiO-x samples were observed in the ultraviolet region. The absorption edge "red shifts" was mainly owing to the formation of the p-n junction at the interface between NiO and TiO_2, band gap overlap, and strong interaction between NiO and TiO_2 in the wavelength range at 350–500 nm. As the NiO content gradually increased, the absorption edge "red shifts" gradually increased and the TiO_2@NiO-8 (TiO_2@NiO-500) had the maximum absorption edge "red shifts" in the experiment range. With the further increase content of NiO, the absorption edge exhibited "blue shift," which was due to the NiO response to ultraviolet light and the excessive NiO coating on the surface of TiO_2 would prevent absorbing visible light for TiO_2, restraining the effect of p-n junction. Meanwhile, the band gap width of NiO was about 3.5 eV and the band gap of TiO_2@NiO was significantly lower than that of the pure phase TiO_2, as shown in Figs. 7b and 8b. Among these photocatalysts, the sample TiO_2@NiO-8 exhibited the lowest band gap. Therefore, the spectral absorption of TiO_2@NiO-8 was more conducive to improve the photocatalytic performance.

The photocurrent response can be used to test the separation efficiency of the photo-induced electron-hole pair, and the electrochemical impedance spectrum can be used to characterize the reaction rate and the electrode resistance. Figure 9 showed the photocurrent and EIS of TiO_2@NiO-x sample. Firstly, we considered the influence of temperature on the separation efficiency. When the temperature raised from 400 to 600 °C, the response strength of the photocurrent increased first and then decreased. Among these photocatalysts, the response strength of the TiO_2@NiO-500 (TiO_2@NiO-8) was the highest (as shown in Fig. 9a). Similarly, the radius of the arc in the EIS decreased first and then increased as the temperature increased, as shown in Fig. 9b. It was shown that the samples with 500 °C (TiO_2@NiO-8) calcination had the highest photoelectron-hole separation efficiency and the minimum electrochemical impedance. The reason was that the TiO_2@NiO-500 had higher crystalline and no other impurity phase was generated at this calcinations temperature. The photocurrent response curve and EIS of pure TiO_2 and TiO_2@NiO-x (x = 2, 4, 6, 8, 10) composite photocatalyst were displayed in Fig. 9c and d. It can be seen from Fig. 9c that the photocurrent response strength of TiO_2@NiO was obviously enhanced compared with the pure-TiO_2, indicating the increasing photoelectron-hole separation efficiency of the TiO_2@NiO photocatalyst. As the increasing NiO content, the response strength of the photocurrent increased first and then decreased. The strength of the sample TiO_2@NiO-8 was higher than any others, which indicated that the separation efficiency of the photocatalyst was the fastest. Similarly, the radius of the EIS was decreased first and then increased with the increasing NiO content. The radius of the circular of the sample TiO_2@NiO-8 was the smallest. This result was coincided with the test results of transient photocurrent response.

Photocatalysis degradation to Rh B of TiO_2@NiO with different amounts of NiO under ultraviolet light irradiation was shown in Fig. 10a and c. The adsorption-desorption equilibrium of the photocatalyst was reached after 30 min under the dark condition. Comparing with P25 and pure TiO_2, the TiO_2@NiO-x exhibited the better adsorption properties. This fact indicated that the NiO nanoparticles coating on the surface of TiO_2 provided a larger specific surface area for Rh B absorption. The result was verified by N_2 absorption and desorption isotherms of the TiO_2@NiO-x, as shown in Fig. 11. The N_2 absorption of the TiO_2@NiO-x was higher than that

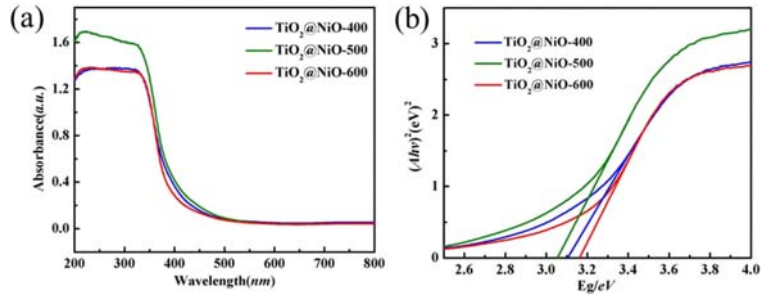

Fig. 7 UV-vis absorption spectra (**a**) and plots of $(A\nu)^2$ versus (ν) (**b**) of TiO_2@NiO-8 calcination at different temperatures

of P25 and pure TiO_2, indicating the specific surface area of TiO_2@NiO-x larger. After ultraviolet light irradiation for 70 min, the photocatalytic performance of TiO_2@NiO-25 was inferior to pure-TiO_2 (as shown in Fig. 10a), which might be due to the excessive NiO limiting the exposure of p-n junction, and the main materials contacted with Rh B were NiO. As the amount of NiO in the TiO_2@NiO photocatalyst gradually decreased, the degradation ability of the photocatalyst was gradually enhanced, such as TiO_2@NiO-20, TiO_2@NiO-15, and TiO_2@NiO-10. Figure 9c further showed the relation of photocatalysis degradation for Rh B with the NiO content in the photocatalyst. It was found that the adsorption rate of pure-TiO_2 was lower than that of all the samples containing NiO. And the adsorption rate in TiO_2@NiO-x was not obvious, which attributed that the surface area variation for TiO_2@NiO-x was not obvious. After UV light irradiation for 70 min of the degradation effect of Rh B in the pure-TiO_2, TiO_2@NiO-2, TiO_2@NiO-4, TiO_2@NiO-6, TiO_2@NiO-8, and TiO_2@NiO-10, samples were 76.4%, 84.5%, 87.97%, 94.9%, 97.9%, and 96.3%, respectively. Among these photocatalysts, the best degradation performance was the TiO_2@NiO-8 photocatalyst. The reaction rate constant k can be calculated according to the kinetic reaction equation $ln(C_0/C) = k \times t$. Figure 10b showed that the reaction rate constants k of pure TiO_2, TiO_2@NiO-25, TiO_2@NiO-20, TiO_2@NiO-15, and TiO_2@NiO-10 were 5.60×10^{-3} min^{-1}, 1.81×10^{-2} min^{-1}, 2.38×10^{-2} min^{-1}, 3.14×10^{-2} min^{-1}, and 4.36×10^{-2} min^{-1}, respectively. In Fig. 10d, the reaction rate constant of pure-TiO_2, TiO_2@NiO-2, TiO_2@NiO-4, TiO_2@NiO-6, TiO_2@NiO-8, and TiO_2@NiO-10 was 1.8×10^{-2} min^{-1}, 2.4×10^{-2} min^{-1}, 2.7×10^{-2} min^{-1}, 3.8×10^{-2} min^{-1}, 5.4×10^{-2} min^{-1}, and 4.3×10^{-2} min^{-1}, respectively. We concluded that the reaction rate of the sample TiO_2@NiO-8 was the fastest, which was consistent with the results of photocurrent response curve and EIS. Under the ultraviolet light irradiation, the degradation efficiency of TiO_2 microspheres after NiO wrapping could be greatly improved. The improvement was mainly due to the high-efficiency photoelectron-hole separation and the extension of the response range. The former was because the formation of p-n junctions between p-type semiconductor NiO and n-type semiconductor TiO_2, which promoted the separation of photoelectron-hole pairs. The latter was due to the charge transition of the electron donor level, and the donor level was formed by the substitution of the 3d orbital of TiO_2 for the conduction band of TiO_2 (Niishiro et al. 2005).

The higher photocatalytic activity of TiO_2@NiO photocatalyst depends not only on higher surface area but also on the separation efficiency of the electron-hole pairs. The higher surface area provides more reactive sites for degradation Rh B, while the higher separation

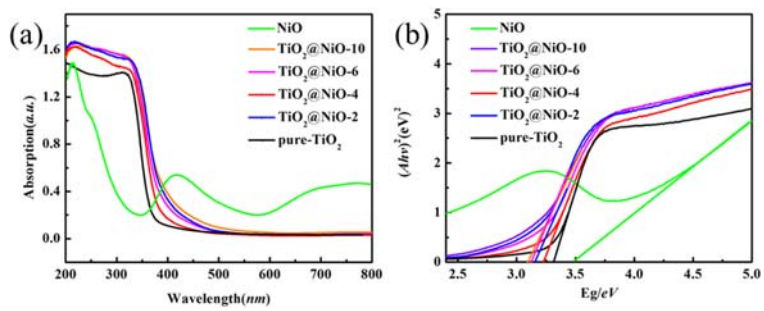

Fig. 8 UV-vis absorption spectra (**a**) and plots of $(A\nu)^2$ versus (ν) (**b**) of NiO and TiO_2@NiO-x (x = 0, 2, 4, 6, 10)

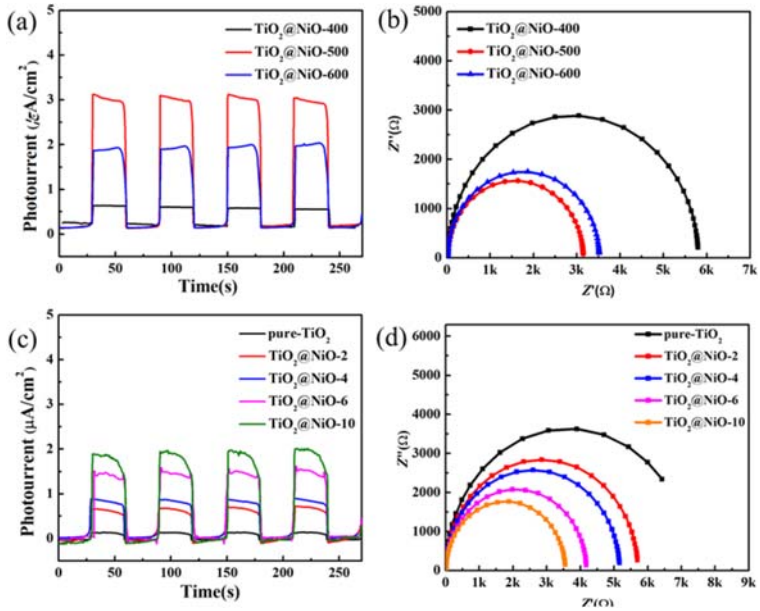

Fig. 9 Photocurrent response (**a**, **c**) and electrochemical impedance spectroscopy (**b**, **d**) of pure-TiO_2 and TiO_2@NiO-x (x = 2, 4, 6, 8, 10)

efficiency of the electron-hole pairs prolongs the lifetime of photoelectron-hole which reacts with H_2O and O_2 further to degraded Rh B. It is well known that the photocatalytic activity of TiO_2 mainly depends on the higher separation efficiency of the electron-hole pairs. When the p-type semiconductor is loaded on the n-type TiO_2, a large amount of p-n junctions are formed at the interface between the TiO_2 and NiO. At equilibrium condition, negative charges are developed on p-type NiO, while positive charge is developed on n-type TiO_2 (R. Vinoth et al. 2017), as demonstrated in Fig. 12. Therefore, the inner electric field is formed at the p-n junction site. Once the TiO_2@NiO photocatalyst is excited by UV light irradiation, electron-hole pairs are generated. Due to the inner electric field, the photogenerated electrons present in the conduction band of NiO migrate into the conduction band of TiO_2 thereby reducing O_2 into O_2^-. Similarly, the photogenerated holes move from

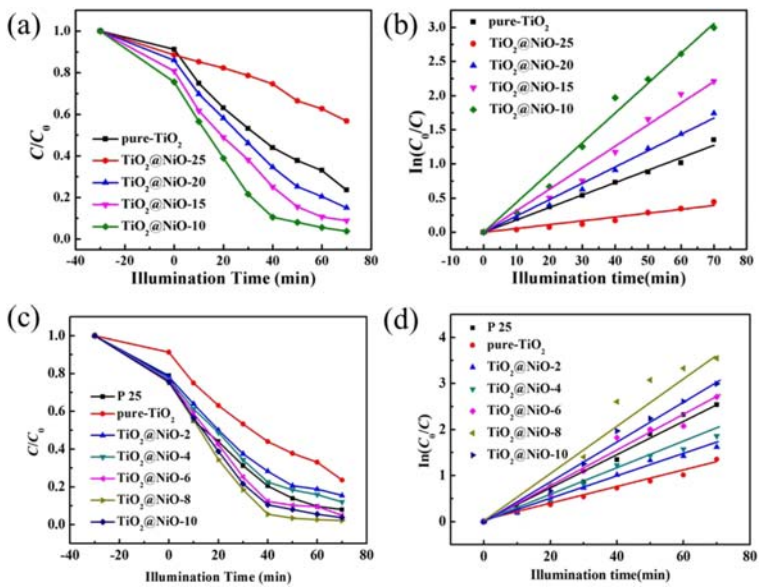

Fig. 10 The photocatalytic degradation Rh B of all samples under ultraviolet irradiation (**a**, **c**). The plots of $\ln(C_0/C)$ vs t of different samples under ultraviolet irradiation (**b**, **d**)

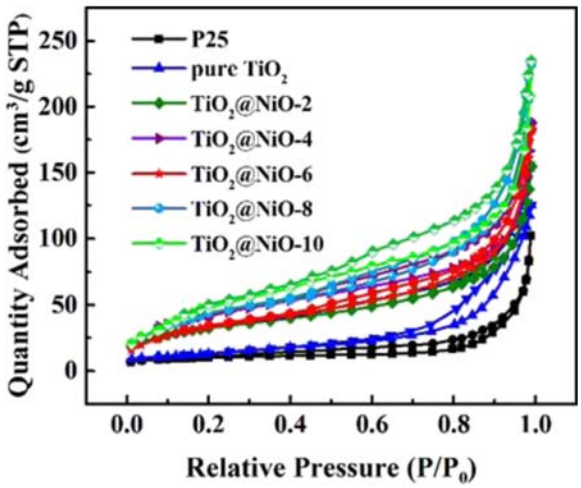

Fig. 11 N_2 absorption and desorption isotherms of P25, pure TiO_2, and TiO_2@NiO-x (x = 2, 4, 6, 8, 10)

valence band of TiO_2 to valence band of NiO and react with H_2O to produce large amount of ·OH radicals. It is well known that the Benzoic is the most commonly used ·OH radical scavenger in the photocatalytic system. As can be seen from Fig. 1s, in the presence of 1 mM benzoic acid, the rate of degradation is significantly decreased. This result clearly attributes that the benzoic acid quenches the ·OH radicals and greatly inhibits the rate of the reaction. Therefore, the ·OH radicals are primarily responsible for the effective degradation of Rh B dye. And the photogenerated electron-hole migrating mechanism indicates that the p-n junction in TiO_2@NiO promotes the separation of electron-hole pairs and enhances the photocatalytic activity.

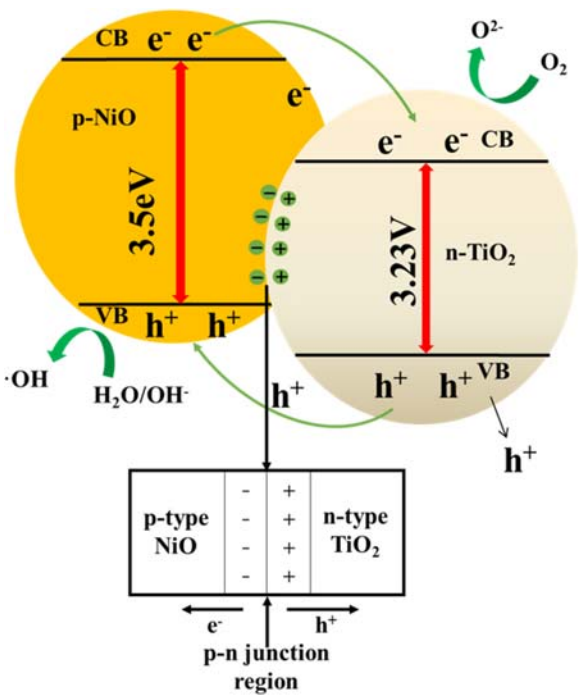

Fig. 12 Schematic illustration of photocatalytic charge transfer mechanism and the energy band structure for TiO_2@NiO

Conclusion

In summary, we synthesized that the TiO_2@NiO photocatalyst by hydrothermal method combined the calcinations. The results showed that the TiO_2@NiO photocatalyst calcined at 500 °C exhibited high crystalline and no impurity phase. Because of the formation of p-n junction between NiO and TiO_2, the recombination of electron-hole in the TiO_2@NiO photocatalyst was prevented, which resulted into the higher photodegradation efficiency than pure TiO_2. The photoelectric performance test confirmed that the TiO_2@NiO-8 photocatalyst had the highest photo-carrier separation efficiency and exhibited the highest degradation rate for Rh B. Hence, it can be used as an efficient strategy for TiO_2 photocatalyst to significant upgrading the photochemical performance.

Funding information This work was financially supported by the Natural Science Foundation of Shaanxi (2015JM213), the Natural Science Basic Research Plan in Shaanxi Province of China (Grant no. 2018JQ2069), and the Postgraduate Innovation Fund of Shaanxi University of Science and Technology.

Compliance with ethical standards

Conflict of interest The authors declare that they have no conflict of interest.

References

Bastian M, Kai H, Guido M (2018) Driving surface redox reactions in heterogeneous photocatalysis: the active state of illuminated semiconductor supported nanoparticles during overall water-splitting. ACS Catal 8(10):9154–9164

Cao T, Li Y, Wang C, Shao C, Liu Y (2011) A facile in situ hydrothermal method to $SrTiO_3/TiO_2$ nanofiber heterostructures with high photocatalytic activity. Langmuir 27(6):2946–2952

Chen S, Sujuan Z, Wei L, Wei Z (2008) Preparation and activity evaluation of p–n junction photocatalyst NiO/TiO_2. J Hazard Mater 155:320–326

Chen CC, Wu RJ, Yao IC, Lu CS (2009) Bis (2-chloroethoxy) Methane degradation by TiO_2 photocatalysis: parameter and reaction pathway investigations. J Hazard Mater 172(2): 1021–1032

Fang J, Zhang Y, Zhou Y, Zhao S, Zhang C, Huang M et al (2017) Synthesis of NiO-TiO_2 hybrids/mSiO_2 yolk-shell architectures embedded with ultrasmall gold nanoparticles for enhanced reactivity. Appl Surf Sci 412:616–626

Fominykh K, Tok GC, Zeller P et al (2017) Rock Salt Ni/Co Oxides with unusual nanoscale-stabilized composition as water splitting electrocatalysts. Adv Funct Mater 27(8): 1605121

Gonçalves R, Wender H, Migowski P et al (2017) Photochemical hydrogen production of Ta_2O_5 nanotubes decorated with NiO nanoparticles by modified sputtering deposition. J Phys Chem C 121(11):5855–5863

Gupta, Shipra, Mital, Tripathi, Manoj (2011) A review of TiO_2 nanoparticles. Sci Bull 56(16):1639

He X, Wang F, Liu H, Niu L, Wang X (2018) Synthesis and color properties of the TiO_2@$CoAl_2O_4$ blue pigments with low cobalt content applied in ceramic glaze. J Am Ceram Soc 101(6):2578–2588

Hou L, Li S, Lin Y et al (2016) Photogenerated charges transfer across the interface between NiO and TiO_2 nanotube arrays for photocatalytic degradation: a surface photovoltage study. J Colloid Interface Sci 464:96–102

Huang W, Harnagea C, Tong X et al (2019) Epitaxial Bi_2FeCrO_6 Multiferroic thin film photoanodes with ultrathin p-type NiO layers for improved solar water oxidation. ACS Appl Mater Interfaces 11(14):13185–13193

Jiang G, Wang R, He J, Wang Y, Sun X, Wang S et al (2011) Preparation of Cu_2O/TiO_2 composite porous carbon microspheres as efficient visible light-responsive photocatalysts. Powder Technol 212(1):284–288

Khun K, Ibupoto ZH, Willander M (2013) Development of fast and sensitive ultraviolet photodetector using p-type NiO/n-type TiO_2 heterostructures. Phys Status Solidi 210(12):2720–2734

Laguna H, Murcia J, Rojas H et al (2019) Differences in the catalytic behavior of Au-metalized TiO_2 systems during phenol photo-degradation and CO oxidation. Catalysis 9(4):331

Lin J, Shen J, Wang R, Cui J, Zhou W, Hu P et al (2011) Nano-p-n junctions on surface-coarsened TiO_2 nanobelts with enhanced photocatalytic activity. J Mater Chem 21(13):5106–5113

Liu H, Su X, Duan C, Dong X, Zhu Z (2014a) A novel hydrogen peroxide biosensor based on immobilized hemoglobin in 3D flower-like MoS_2 microspheres structure. Mater Lett 122(5): 182–195

Liu R, Yoshida H, Fujita S, Arai M (2014b) Photocatalytic hydrogen production from glycerol and water with NiO_x/TiO_2 catalysts. Appl Catal B Environ 144:41–45

Mcintyre NS, Cook MG (1975) X-ray photoelectron studies on some oxides and hydroxides of cobalt, nickel, and copper. Anal Chem 47(13):2208–2213

Niishiro R, Kato H, Kudo A (2005) Nickel and either tantalum or niobium-codoped TiO_2 and $SrTiO_3$ photocatalysts with visible-light response for H_2 or O_2 evolution from aqueous solutions. Phys Chem Chem Phys 7(10):2241–2245

Oropeza FE, Egdell RG (2011) Control of valence states in Rh-doped TiO_2 by Sb Co-doping: a study by high resolution X-ray photoemission spectroscopy. Chem Phys Lett 515(4): 249–253

Pan X, Yang MQ, Fu X, Zhang N, Xu YJ (2013) Defective TiO_2 with oxygen vacancies: synthesis, properties and photocatalytic applications. Nanoscale 5(9):3601–3614

Pham TD, Lee BK (2014) Cu doped TiO_2/GF for photocatalytic disinfection of Escherichia coli in bioaerosols under visible light irradiation: application and mechanism. Appl Surf Sci 296(4):15–23

Rupa AV, Divakar D, Sivakumar T (2009) Titania and noble metals deposited titania catalysts in the photodegradation of Tartazine. Catal Lett 132(1):259–267

Sun H, Dong B, Su G et al (2015a) Towards TiO_2 nanotubes modified by WO_3 species: influence of exsitu crystallization of precursor on the photocatalytic activities of WO_3/TiO_2 composites. J Phys D-Appl Phys 48(35):355305

Sun H, Dong B, Su G et al (2015b) Modification of TiO_2 nanotubes by WO_3 species for improving their photocatalytic activity. Appl Surf Sci 343:181–187

Sun H, Dong B, Song L et al (2017) High photodegradation ability of dyes by Fe(III)-tartrate/TiO_2 nanotubular photocatalyst supported via photo-fenton reaction. J Photochem Photobiol A Chem 334:20–25

Vimonses V, Bo J, Chow CWK, Saint C (2010) An adsorption-photocatalysis hybrid process using multi-functional-nanoporous materials for wastewater reclamation. Water Res 44(18):5385–5397

Vinoth R, Karthik P, Devan K, Neppolian B, Ashokkumar M (2016) TiO_2-NiO p-n Nanocomposite with enhanced sonophotocatalytic activity under diffused sunlight. Ultrasonics-Sonochemistry 35:655–663

Vinoth R, Karthik P, Devan K, et al. (2016) TiO2-NiO p-n nanocomposite with enhanced photocatalytic activity under diffused sunlight[J]. Ultrasonics Sonochemistry 35:655–663

Wang C, Shao C, Zhang X, Liu Y (2009) SnO_2 Nanostructures-TiO_2 nanofibers heterostructures: controlled fabrication and high photocatalytic properties. Inorg Chem 48(15):7261

Wang M, Hu Y, Han J et al (2015) TiO_2/NiO hybrid shells: p-n junction photocatalysts with enhanced activity under visible light. J Mater Chem A 3(41):20727–20735

Wang M, Han J, Hu Y et al (2016) Carbon-incorporated NiO/TiO_2 mesoporous shells with p-n heterojunctions for efficient visible light photocatalysis. ACS Appl Mater Interfaces 8: 29511–29521

Wang J, Mao S, Liu Z et al (2017) The dominating role of Ni0 on the interface of Ni/NiO for enhanced hydrogen evolution reaction.[J]. ACS Appl Mater Interfaces 9(8):7139

Wang K, Peng T, Wang Z et al (2019) Correlation between the H_2 response and its oxidation over TiO_2 and N Doped TiO_2 under UV irradiation induced by fermi level. Appl Catal B Environ 250:89–98

Xian J, Li D, Chen J, Li X, He M, Shao Y et al (2014) TiO_2 nanotube array-graphene-CdS quantum dots composite film in Z-scheme with enhanced photoactivity and photostability. ACS Appl Mater Interfaces 6(15):13157–13166

Yap PS, Lim TT (2011) Effect of aqueous matrix species on synergistic removal of bisphenol-A under solar irradiation

using nitrogen-doped TiO_2/AC composite. Appl Catal B Environ 101(3-4):709–717

Yu C, Bai Y, Yan D, Li X, Zhang W (2014a) Improved electrochemical properties of Sn-doped TiO_2 nanotube as an anode material for lithium ion battery. J Solid State Electrochem 18(7):1933–1940

Yu L, Li Z, Liu Y, Cheng F, Sun S (2014b) Mn-doped CdS quantum dots sensitized hierarchical TiO_2 flower-rod for solar cell application. Appl Surf Sci 305(7):359–365

Zhang Z, Shao C, Li X (2013) Hierarchical assembly of ultrathin hexagonal SnS_2 nanosheets onto electrospun TiO_2 nanofibers: enhanced photocatalytic activity based on photoinduced interfacial charge transfer. Nanoscale 5(2):606–618